Available online at www.sciencedirect.com
ScienceDirect
Scripta Materialia 57 (2007) 865–868
Scripta MATERIALIA
www.elsevier.com/locate/scriptamat

Coupling effect of multiple precipitates on the ductile fracture of aged Al–Mg–Si alloys

S.P. Yuan,[a] G. Liu,[a] R.H. Wang,[a] X. Pu,[a] G.-J. Zhang,[a] J. Sun[a,*] and K.-H. Chen[b]

[a] *State Key Laboratory for Mechanical Behavior of Materials, School of Material Science and Engineering, Xi'an Jiaotong University, Xi'an 710049, China*
[b] *State Key Laboratory for Powder Metallurgy, The University of Southern Central China, Changsha 410083, China*

Received 19 May 2007; revised 21 June 2007; accepted 26 June 2007
Available online 10 August 2007

The coupling effect of multiple precipitates on the mechanical properties of an Al–Mg–Si alloy was investigated by experiment and modeling. A density-dependent superposition effect of multiple precipitates on yield strength was observed, differing from simple addition. Using a multiscale fracture model, the coupling effect of multiple precipitates on the strain to fracture was also revealed to be a density-dependent superposition of the individual types of precipitate, essentially similar to that for yield strength.

Keywords: Aluminum alloys; Multiple precipitates; Coupling effect; Mechanical properties; Modeling

There has been increasing interest in establishing quantitative relationships between the mechanical properties and the technical parameters of aging treatment, such as aging temperature and aging time [1,2]. Since the pioneer work of Shercliff and Ashby [3], many efforts have been made to model the variation of hardness or yield strength of aluminum alloys during aging treatment and significant progress has been achieved in predicting the yield strength with respect to aging temperature and aging time [4–11]. Most recently, some of the present authors [12–15] have studied the ductility and fracture toughness of aged aluminum alloys by using a multiscale model that considers all the influences coming not only from the aging-dependent nanometer-sized precipitates but also from the other two kinds of larger second-phase particles, i.e. micrometer-sized constituents and submicrometer-sized dispersoids, both of which seriously affect the ductile fracture of aluminum alloys [16,17]. These achievements make it possible to obtain the expected mechanical properties for aluminum alloys using prediction-assisted design of the aging treatment.

For simplification, almost all the earlier modeling work was based on the assumption of a single type of precipitate. But in practice, multiple precipitates, with different characteristics and/or different shapes, usually coexist in the aged aluminum alloys due to the complex composition and complicated aging processing [18]. Some experiments and computer simulations [19–21] have been carried out to investigate the superposition of strengthening effects of different precipitates. However, there has been no report, to the authors' best knowledge, on the coupling effect of multiple precipitates on the ductile fracture of the aged aluminum alloys.

In this paper, both experiments and analytical modeling were performed to study the coupling effect of multiple precipitates on the ductile fracture of an aged Al–Mg–Si alloy. As a potential material for use in the automobile industry, Al–Mg–Si alloys usually undergo a two-step aging-hardening process (pre-aging treatment is employed to form "seeds" for the precipitates to assist the formation of effective hardening precipitates upon a short second heating [22]) and contain multiple precipitates [23–25]. Here, experiments were focused on the evolution of multiple precipitates in a secondary aging treatment and their influence on the yield strength and ductility of the Al–Mg–Si alloy. A multiscale model [12–15] was modified to estimate the influence of multiple precipitates on ductility.

The Al–Mg–Si alloys used in present investigation are extruded rods of 18 mm in diameter. The composition is 1.12 wt.% Mg, 0.57 wt.% Si, 0.25 wt.% Cu, 0.22 wt.% Cr, and the balance Al. The alloys had been solution-treated at 703 K for half an hour followed by water

* Corresponding author. Tel.: +86 29 82667143; fax: +86 29 82663453; e-mail: junsun@mail.xjtu.edu.cn

1359-6462/$ - see front matter © 2007 Acta Materialia Inc. Published by Elsevier Ltd. All rights reserved.
doi:10.1016/j.scriptamat.2007.06.063

quenching and then pre-aged at 373 K for 20 min. After storing at room temperature for fifty months, the alloys were secondarily aged at 473 K for a series of times from 2 to 40 h. The yield strength and strain to fracture of the differently aged alloys were measured by using the smooth dog-bone-shaped tensile specimens having a gauge size of 6 mm in diameter and 40 mm in length. Details of the microstructural analyses can be found in our previous papers [11–15].

Figure 1a shows the microstructure of the sample before the secondary aging treatment, where the spherical second-phase particles, determined as metastable pre-β'' phase of $AlMg_4Si_6$ [26], were precipitated during the first aging treatment and subsequently grow during the following storage period. In the secondary aging treatment, it was found that the sphere pre-β'' precipitates decrease gradually. On the other hand, two other kinds of strengthening second-phase particles were being precipitated, which are rod-shaped and needle-shaped precipitates, respectively, as typically shown in Figure 1b. The rod-shaped precipitates, determined as the metastable β'' phase of Mg_5Si_6, formed in situ on the pre-β'' phase and grew by consuming the pre-β'' phase, while the needle-shaped strengthening particles, determined as the metastable β' phase of Mg_2Si, were precipitated from the matrix. The precipitation sequence is in good agreement with previous results [27]. During the whole of the secondary aging treatment, the three kinds of precipitates are observed to coexist, so that the Al–Mg–Si alloys contain multiple precipitates.

Figure 2a shows the experimentally determined size evolution of both β'' particles and β' particles, where r and l refer to the radius (open circles) and half-length (solid circles) of the rod- or needle-shaped precipitates [11], respectively. Fitting lines indicate that the size variation of rod-shaped β'' particles follows the $t^{0.25}$ law (t: aging time, in hours), i.e. r (l) $= A \times t^{0.25}$ (nm), where the constant A is calibrated as about 4.4 for r and 30 for l. On the other hand, the dependence of the average size of the needle-shaped β' particles on t exhibit the relationship r (l) $= B \times t^{0.1}$ (nm), with $B = 2.9$ for r and 29 for l. The much lower value (0.1) for the growth exponent of the β' particles may be related to the exhausted matrix where most of the excess solute atoms have been provided for the long-time growth of pre-β'' particles. As to the spherical pre-β'' particles, except those used for

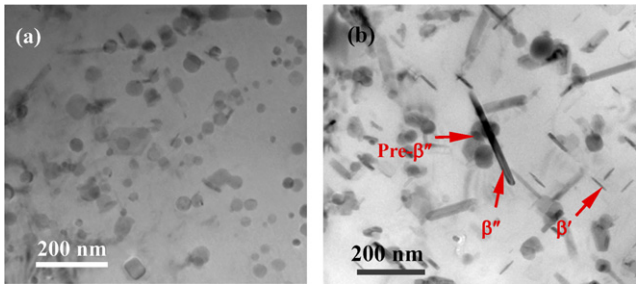

Figure 1. Typical TEM images showing the morphology and size of pre-β'' precipitates of $AlMg_4Si_6$ before secondary aging treatment (a) and of multiple precipitates, i.e. spherical pre-β'' particles of $AlMg_4Si_6$, rod-shaped β'' precipitates of Mg_5Si_6, and needle-shaped β' precipitates of Mg_2Si, after secondary aging treatment (b).

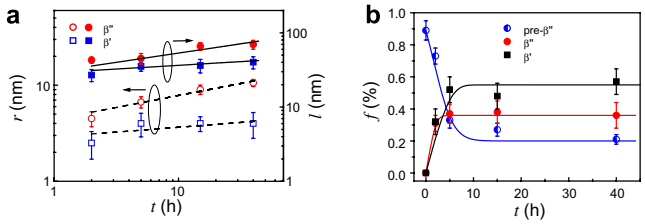

Figure 2. (a) Variation of the average size (radius r and half-length l) of the β'' precipitates (circles) and β' precipitates (squares) with aging time (t) and (b) variation of the volume fraction (f) of the pre-β'' precipitates (half-close circles), β'' precipitates (closed circles) and β' precipitates (squares) with t. Fitting lines are presented for quantitative description.

in situ nucleation and growth of β'' particles, the average radius is almost constant at 15 nm during the whole aging treatment.

Because some pre-β'' particles are dissolved to provide solute atoms for the growth of β'' particles, the pre-β'' particles exhibit a gradual decrease in volume fraction, as shown in Figure 2b. On the other hand, the volume fraction of both β'' particles and β' particles increases sharply at the early aging course and subsequently exhibit a somewhat slight change, which is believed to result from the entire consumption of the excess solute atoms in the matrix in combination with surviving pre-β'' particles achieving thermodynamic stability. To a first approximation, all the volume fraction evolutions of the three kinds of precipitates should follow an Avrami type [28] or quasi-Avrami type relationship, i.e. $f_s = 0.89 - 0.69 \times \{1 - \exp[-(t/t_0)^{1.5}]\}$ ($t_0 = 3.59$ h) for sphere- shaped pre-β'' particles, $f_r = 0.36 \times \{1 - \exp[-(t/t_0)^{1.5}]\}$ ($t_0 = 0.94$ h) for rod-shaped β'' particles, and $f_n = 0.55 \times \{1 - \exp[-(t/t_0)^{1.5}]\}$ ($t_0 = 1.79$ h) for needle-shaped β' particles. These isothermal phase transition kinetics curves are very similar to our previous results on the same Al–Mg–Si alloys [29]. Further analyses in Figure 2b also reveal that the sum of volume fraction of the three kinds of precipitates exhibit only a slight change during the whole aging treatment.

Accompanying the evolution of the multiple precipitates, there is a visible change in the mechanical properties of the Al–Mg–Si alloy, as seen in Figure 3, where a and b show the variation of yield strength (σ_y) and the strain to fracture (ε_f) (both as solid circles) with aging time t, respectively. It is surprisingly found that the long storage after pre-aging treatment make the alloy even exhibit a decrease trend in yield strength in the second aging treatment, as shown in Figure 3a. This is mainly attributed to the fact that the pre-β'' phase particles precipitated in the pre-aging treatment have grown into effective hardening particles during the long storage and the application of secondary aging treatment caused the partial dissolution of pre-β'' particles to form less-strengthening β'' particles. On the other hand, the ductility or the strain to fracture increases remarkably in the second aging treatment, coinciding well with the traditional law that strength and ductility are mutually opposite.

The overall yield strength (σ_y) of aged aluminum alloys has contributions from the intrinsic yield strength (σ_i) of

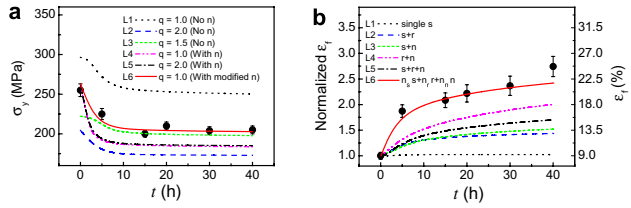

Figure 3. Dependence of (a) yield strength (σ_y) and (b) the strain to fracture (ε_f) on t. Circles are experimental results and lines are calculated results. In (a), Lines 1–3 were come from Eq. (1a) with $q = 1.0$, 2.0, and 1.5, respectively; Lines 4 and 5 from Eq. (1b) with $q = 1.0$ and 2.0, respectively; and Line 6 from revised Equation (1b) by incorporating the strengthening effect of the pre-β'' precipitates with that of the β'' precipitates. In (b), the left vertical axis is normalized ε_f, as the same treatment in previous papers [12–14]. Lines 1–6 are the results calculated by considering a series of possible coupling effects of the multiple precipitates, as detailed in the text.

pure aluminum alloys, solid solution hardening caused by the elements Mg, Si, and Cu ($\sigma_k = \sum_j k_j C_j^{2/3}$) [30], where $j =$ Mg, Si, and Cu, C_j is the concentration of a specific alloying element in solid solution, and k_j is the corresponding scaling factor as $k_{Mg} = 29.0$ MPa wt.%$^{-2/3}$, $k_{Si} = 66.3$ MPa wt.%$^{-2/3}$, and $k_{Cu} = 46.4$ MPa wt.%$^{-2/3}$ [31]), and precipitation hardening σ_p^j ($j =$ s, r, and n, which corresponds to the contribution from spherical pre-β'' precipitates, rod-shaped β'' precipitates, and needle-shaped β' precipitates, respectively). Detailed expressions for σ_p^s (spherical precipitates) and for σ_p^r and σ_p^n (rod- or needle-shaped precipitates) can be found in Ref. [9] and Refs. [11,32], respectively.

It has been known that, if two or more types of strengthening obstacles are present in the matrix, the total critical resolved shear stress (CRSS), τ, of the materials will be a superposition of the strengthening of the individual types of strengthening obstacles. A general approximation for the strengthening due to N obstacles is $(\tau_\sum)^q = \sum_{j=1}^N (\tau_j)^q$, where exponent q has the value between 1 (linear addition law) and 2 (Pythagorean addition law) [19,33]. Recent computer simulation [20] yielded another version as $(\tau_\sum)^q = \sum_{j=1}^N (n_j)^{q/2} (\tau_j)^q$, where the density fraction n_j was introduced ($\sum_{j=1}^N n_j = 1$). Similarly, in the present model, the two versions of superposition relationship will both be used to calculate σ_y, i.e.

$$\sigma_y = \sigma_i + \left(\sum_j (\sigma_j)^q \right)^{1/q}, \quad j = \mathrm{k, s, r, n} \tag{1a}$$

$$\sigma_y = \sigma_i + \left((\sigma_k)^q + \sum_j (n_j)^{q/2} (\sigma_j)^q \right)^{1/q}, \quad j = \mathrm{s, r, n} \tag{1b}$$

with Eq. (1b) considering the weight effect of the relative volume fraction of the multiple precipitates.

The calculated results by using Eq. (1) were depicted in Figure 3a as lines. The Lines 1–3 come from Eq. (1a) with $q = 1.0$ (dotted line), 2.0 (dashed line), and 1.5 (short-dashed line), respectively. Lines 4 and 5 come from Eq. (1b) with $q = 1.0$ (dash-dot-dot line), and 2.0 (dash-dot line), respectively. Unfortunately not all the lines fit the experimental results well. However, when considering the in situ formation of β'' precipitates on the pre-β'' precipitates and the obstacle position not changed before and after phase transformation, it is reasonable to incorporate the strengthening effect of the pre-β'' precipitates with that of the β'' precipitates. This means that the term $(n_s + n_r)^{q/2}(\sigma_s + \sigma_r)^q$ could be used in Eq. (1b), which yields calculation results fitting well with the experimental results when $q = 1$, as shown in Figure 3a as Line 6 (solid line). The successful employment of revised Eq. (1b) indicates that this equation is essentially feasible for describing the superposition of multiple precipitates but that some revisions are required when a more complicated relationship exists between the multiple precipitates, such as the in situ phase transformation in the present case.

As to the strain to fracture ε_f, it is revealed by our multiscale fracture model that it is closely depend on the parameters of differently sized second phase particles, i.e. micrometer-sized constituents, submicrometer-sized dispersoids, and nanometer-sized precipitates, as

$$\varepsilon_f = \frac{1}{\tilde{\varepsilon}_E(\theta)} \left[\frac{I}{0.405\pi h} \right]^{\frac{1}{n+1}} \left[\frac{\lambda_c}{2r_c} - 1 \right]^{\frac{1}{n+1}} \frac{\sqrt{(\varepsilon_d)^2 + \sum_j (\varepsilon_j)^2}}{2}, \quad j = \mathrm{s, \ and/or\ } r, \ \mathrm{and/or\ } n, \tag{2}$$

where r_i and λ_i ($i =$ c, d, j) are the size and interparticle spacing of constituents, dispersoids, and precipitates, respectively; ε_d is the local strain associated with the geometrically necessary dislocations caused by the incompatibility in shape change between matrix and dispersoids in deformation, and ε_j is that related to j precipitates; $\tilde{\varepsilon}_E(\theta)$ is the effective value for the normalized coefficient $\tilde{\varepsilon}_{ij}(\theta)$ and is a constant when $\theta = 0$, n is the strain hardening exponent, and I and h are functions of n [14].

The geometrically necessary dislocations caused by multiple precipitates may be superposed or covered by the overwhelming one, depending on the relative size and interparticle spacing between the multiple precipitates. Therefore, a series of possible coupling effects of the multiple precipitates will be considered. The first one is to consider only the influence of spherical pre-β'' precipitates. For this situation, expressions for ε_d and ε_s can be found in Ref. [14], by which Eq. (2) gives Line 1 (dotted line) in Figure 3b. Secondly, the combination of any two types of precipitates is considered, where ε_d and ε_j are given as

$$\varepsilon_d = 1.7 r_d b \frac{\lambda_i \lambda_j}{\lambda_d \lambda_i + \lambda_d \lambda_j + \lambda_i \lambda_j} \rho_g^c,$$
$$\varepsilon_i = 0.25 \lambda_i b \frac{\lambda_d \lambda_j}{\lambda_d \lambda_i + \lambda_d \lambda_j + \lambda_i \lambda_j} \rho_g^c, \quad (i, j) = (\mathrm{s, r}), \ \mathrm{or}\ (\mathrm{s, n}), (\mathrm{r, n}) \tag{3}$$

where ρ_g^c is the critical density of geometrically necessary dislocations in the Al matrix. By using both Eqs. (2) and (3), Lines 2–4 in Figure 3b are obtained to show the coupling effect of spherical pre-β'' precipitates (s) + rod-shaped β'' precipitates (r) (dashed line), s + needle-shaped β' precipitates (n) (short-dashed line), and (r + n) (dash–dot–dot line), respectively. In addition, the coupling effect of all three kinds of precipitates can be calculated following a similar treatment and the

results are also depicted in Figure 3b as Line 5 (dash–dot line). Comparing the calculations with experimental results, it is found that all the above fine lines fail in fitting the measured ones. However, if one is referring to the treatment in modeling yield strength (see Eq. (1b)) and considering the weight effect of density fraction of multiple precipitates on ductile fracture, Eq. (2) could be rewritten as

$$\varepsilon_f = \frac{1}{\tilde{\varepsilon}_E(\theta)}\left[\frac{I}{0.405\pi h}\right]^{\frac{1}{n+1}}\left[\frac{\lambda_c}{2r_c}-1\right]^{\frac{1}{n+1}}\frac{\sqrt{(\varepsilon_d)^2+\sum_j(n_j)(\varepsilon_j)^2}}{2}, \quad j = \mathrm{s,r,\ and\ n} \tag{4}$$

This equation produces results that are in good agreement with the experiments, as shown in Figure 3b as Line 6 (solid line). It is then clearly revealed that the coupling effect of multiple precipitates on ε_f is also a density-dependent superposition of the individual kind of precipitates, essentially similar to that on σ_y. Some in-depth investigations are being undertaken for a more comprehensive understanding.

In summary, experiments and multiscale modeling have been performed to investigate the coupling effect of multiple precipitates on yield strength and strain to fracture in an aged Al–Mg–Si alloy. The density-dependent superposition effect of multiple precipitates on yield strength has been observed, supporting the previous computer calculations. Besides, the coupling effect of multiscale precipitates on the strain to fracture is found to be another density-dependent superposition effect of the individual types of precipitate.

This work was supported by the National Basic Research Program of China (Grant No. 2004CB619303 and 2005CB623700), the National Natural Science Foundation, and the National Outstanding Young Investigator Grant of China. The work was also supported by the 111 Project of China under Grant No. B06025, Program for Changjiang Scholars and Innovative Research Team in University (PCSIRT) as well as Science and Technology Key Project from Ministry of Education of China under Grant Nos. 02182 and 03182.

[1] E. Hornbogen, E.A. Starke Jr., Acta Metall 41 (1993) 1.
[2] Ø. Grong, H.R. Shercliff, Prog. Mater. Sci. 47 (2002) 163.
[3] H.R. Shercliff, M.F. Ashby, Acta Mater. 38 (1990) 1789.
[4] D.H. Bratland, Ø. Grong, H. Shercliff, O.R. Myhr, S. TjØtta, Acta Metall. 45 (1997) 1.
[5] O.R. Myhr, Ø. Grong, Acta Mater. 48 (2000) 1605.
[6] M.J. Starink, S.C. Wang, Acta Mater. 51 (2003) 5131.
[7] M. Nicolas, A. Deschamps, Acta Mater. 51 (2003) 6077.
[8] S. Esmaeili, D.J. Lloyd, W.J. Poole, Acta Mater. 51 (2003) 3467.
[9] A. Deschamps, Y. Brechet, Acta Mater. 47 (1999) 293.
[10] M.J. Starink, P. Wang, I. Sinclair, P.J. Gregson, Acta Mater. 47 (1999) 3855.
[11] G. Liu, G.J. Zhang, X.D. Ding, J. Sun, K.H. Chen, Mater. Sci. Eng. A344 (2003) 113.
[12] G. Liu, J. Sun, C.W. Nan, K.H. Chen, Acta Metall. 53 (2005) 3459.
[13] G. Liu, G.J. Zhang, R.H. Wang, W. Hu, J. Sun, K.H. Chen, Acta Metall. 55 (2007) 273.
[14] G. Liu, G.J. Zhang, X.D. Ding, J. Sun, K.H. Chen, Metall. Mater. Trans. 35A (2004) 1725.
[15] G. Liu, G.J. Zhang, X.D. Ding, J. Sun, K.H. Chen, Mater. Sci. Technol. 19 (2003) 887.
[16] G.T. Hahn, A.R. Rosenfield, Metall. Trans. 6A (1975) 653.
[17] G.G. Garrett, J.F. Knott, Metall. Trans. 9A (1978) 1187.
[18] E. Clouet, L. Lae, T. Epicier, W. Lefebvre, M. Nastar, A. Deschamps, Nature Mater. 5 (2006) 482.
[19] J.C. Huang, A.J. Ardell, Acta Mater. 36 (1988) 2995.
[20] A.W. Zhu, A. Csontos, E.A. Starke Jr., Acta Mater. 47 (1999) 1713.
[21] A.W. Zhu, B.M. Gable, G.J. Shiflet, E.A. Starke Jr., Acta Mater. 52 (2004) 3671.
[22] J.H. Chen, E. Costan, M.A. van Huis, Q. Xu, H.W. Zandbergen, Science 416 (2006) 312.
[23] D.J. Chakrabarti, David E. Laughlin, Prog. Mater. Sci. 49 (2004) 389.
[24] C. Ravi, C. Wolverton, Acta Mater. 52 (2004) 4213.
[25] C.S. Tsao, C.Y. Chen, U.S. Jeng, T.Y. Kuo, Acta Mater. 54 (2006) 4621.
[26] S.P. Yuan, G. Liu, R.H. Wang, X. Pu, G.J. Zhang, J. Sun, in preparation.
[27] H.W. Zandbergen, S.J. Andersen, J. Jansen, Science 277 (1997) 1221.
[28] H.R. Shercliff, M.F. Ashby, Acta Mater. 38 (1990) 1803.
[29] G. Liu, Ph.D. Thesis, Xi'an Jiaotong University, 2002.
[30] F.R.N. Nabarro, Theory of Crystal Dislocation, Oxford University Press, Oxford, 1967.
[31] O.R. Myhr, Ø. Grong, S.J. Anderson, Acta Mater. 49 (2001) 65.
[32] A.W. Zhu, E.A. Starke Jr., Acta Mater. 47 (1999) 3263.
[33] C. Schlieser, E. Nembach, Acta Metall. Mater. 43 (1995) 3983.